# Microwave-Assisted Extraction, Separation, and Chromogenic Detection of Laced Marijuana for Presumptive Point-of-Interdiction Testing

*O'Connell, K.; et al.*

## Supplementary Figures

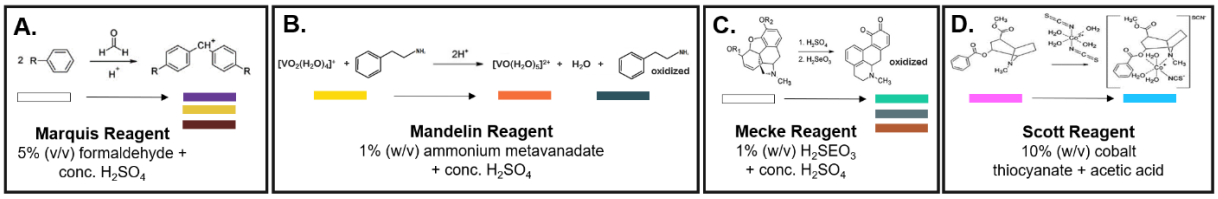


| E. Marquis | Mandelin | Mecke | Scott |
|---|---|---|---|
| MDMA | MDMA | MDMA | Cocaine |
| Amphetamine | Amphetamine | DMT | PCP |
| Methamphetamine | Methamphetamine | Oxycodone | Lidocaine |
| Heroin | PMMA | Heroin | Heroin |
| Morphine | Cocaine | Morphine | |
| Codeine | Codeine | Codeine | |
| Mescaline | Ketamine | Mescaline | Ketamine |
| Fentanyl | Methylone | Methylone | |

**Supplemental Figure 1.** *Illustration of Indicator Reagents with Standard Chromogenic Responses.* **A.** The Marquis reagent is the most frequently employed screening agent, first developed for the detection of morphine, it has since found utility in the detection of amphetamines and synthetic opioids (see column 1 below). However, cross reactions with aspirin and sugar have also been reported. **B.** The Mandelin reagent contains a highly colored transition metal that becomes reduced in the presence of alkaloids. Unlike the Marquis reagent, the Mandelin reagent is capable of detecting Ketamine (see column 2 below), a powerful anesthetic. **C.** The Mecke reagent is most reactive to alkaloids (see column 3 below) and has shown value in distinguishing heroin from fentanyl. **D.** The Scott reagent was originally intended as a highly specific indicator for cocaine but has since gone through several modifications in the literature to address its lack of specificity against various analogs (see column 4 below). **E.** Chart providing detectable controlled substances according to each indicator reagent, including 3,4-methylenedioxymethamphetamine (MDMA), paramethoxymethamphetamine (PMMA), N,N-dimethyltryptamine (DMT), and phencyclidine (PCP). List for each reagent is not exhaustive.

**Microwave-Assisted Extraction, Separation, and Chromogenic Detection of Laced Marijuana for Presumptive Point-of-Interdiction Testing**

*O'Connell, K.; et al.*

Supplementary Figures

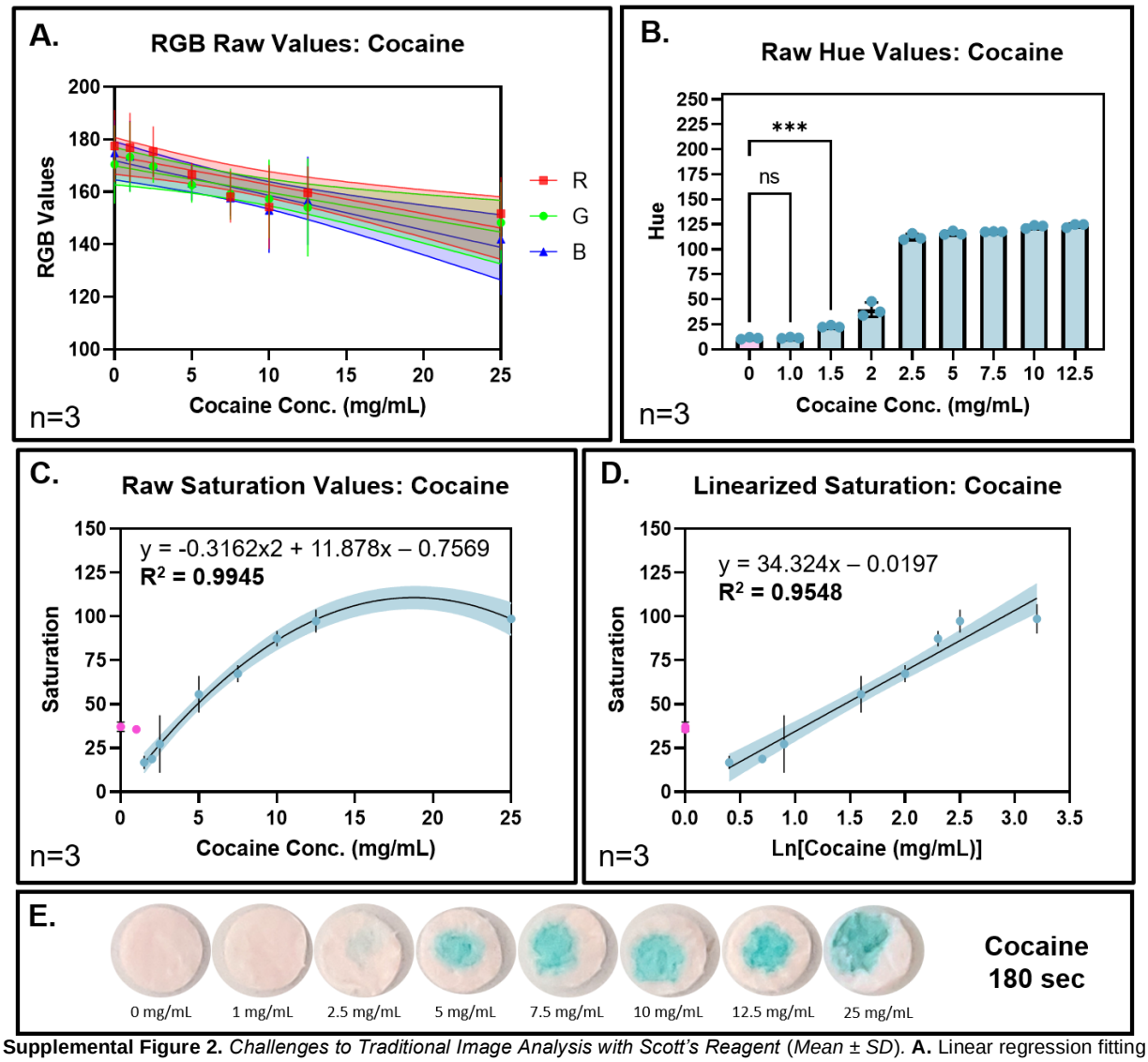


**Supplemental Figure 2.** *Challenges to Traditional Image Analysis with Scott's Reagent* (*Mean* ± *SD*). **A.** Linear regression fitting of RGB image analysis data for cocaine reacted with the Scott's reagent. Shading around the curve represent the 95% Confidence Interval (CI) around the line of best fit. **B.** The average hue values, measured according to image analysis in the HSB color space, for each set of example images is also shown. A Multiple Comparisons Two-Way ANOVA was performed to determine whether the mean hue value of all positive controls differed significantly from a negative control containing only solvent ($\alpha = 0.01$). **C.** Calibration curve of mean squared saturation values for cocaine reacted with Scott's reagent $R^2 = 0.9919$. The line of best fit does not include 0 or 1.0 mg/mL as the saturation value of the negative control (pink) exceeds that of the next lowest concentration positive sample, due to the initial color of the reagent itself. Shading around the curve represent the 95% Confidence Interval (CI) around the line of best fit. **D.** Mean hue values derived from the same samples used for the calibration curve are shown, emphasizing the influence of the background color on results. **E.** Example images of pure standards of **i.** cocaine reacted with the Scott reagent.

**Microwave-Assisted Extraction, Separation, and Chromogenic Detection of Laced Marijuana for Presumptive Point-of-Interdiction Testing**

*O'Connell, K.; et al.*

Supplementary Figures

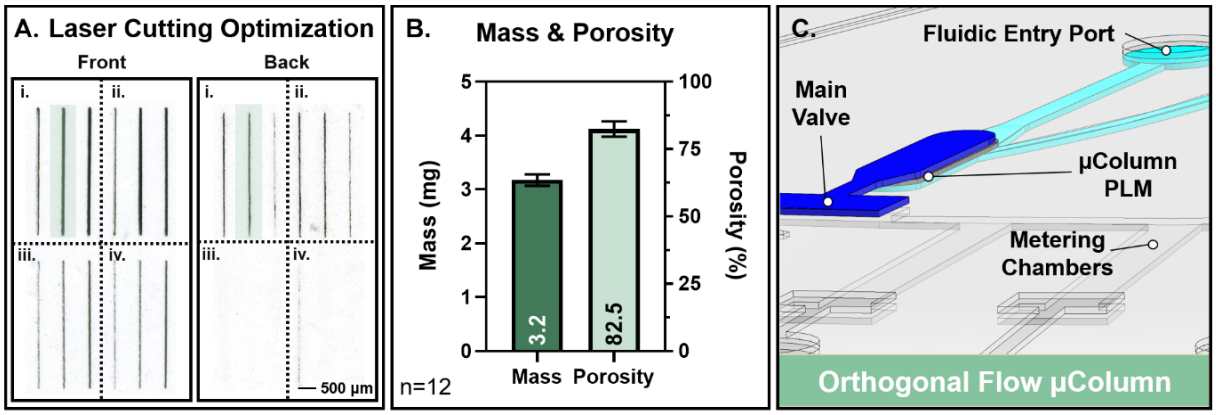


**Supplemtary Figure 3:** *Microdevice Integration of Membrane µColumn.* **A.** Scanned images of laser-cut functionalized membranes used to determine optimal settings. Panels **i.** and **ii.** were cut at 8% power while panels **iii.** and **iv.** were cut at 10% power. All panels were cut at 10% speed. Each line was cut using 1, 2 or 3 laser passes (from left to right within each panel). Optimal laser cut settings of 8% power 10% speed, 2 passes (green box) was selected based on complete cut-through, with a 100% success rate in removal from surrounding material, coupled with minimal edge charring. **B.** A grid composed of 12 µColumn cavities were laser-cut and assembled according to the PCL method. Prior to alignment of the top PET layer, each laser-cut SPE membrane was placed within its allotted cavity, then sealed via lamination. Membrane material was laser-cut according to previously optimized settings and cleaned using compressed air. The mass of each µColumn was measured by subtracting the mass of the grid before and after the addition of each membrane insert (5.2 mm in length, with the arc on either end extending 152.1°). A simplified fluidic architecture, composed of an inlet and outlet port directly above and below the µColumn material (not shown), enabled access to dyed $CH_3OH$ that was added in 0.5 µL increments. The consistency in total mass and membrane porosity across twelve integrated µColumns was evaluated according to a fine mass balance and the max volume of liquid that could be added just prior to overflow. **C.** SolidWorks rendering of orthogonal flow design through the integrated Particle Loaded Membrane (PLM) µColumn.

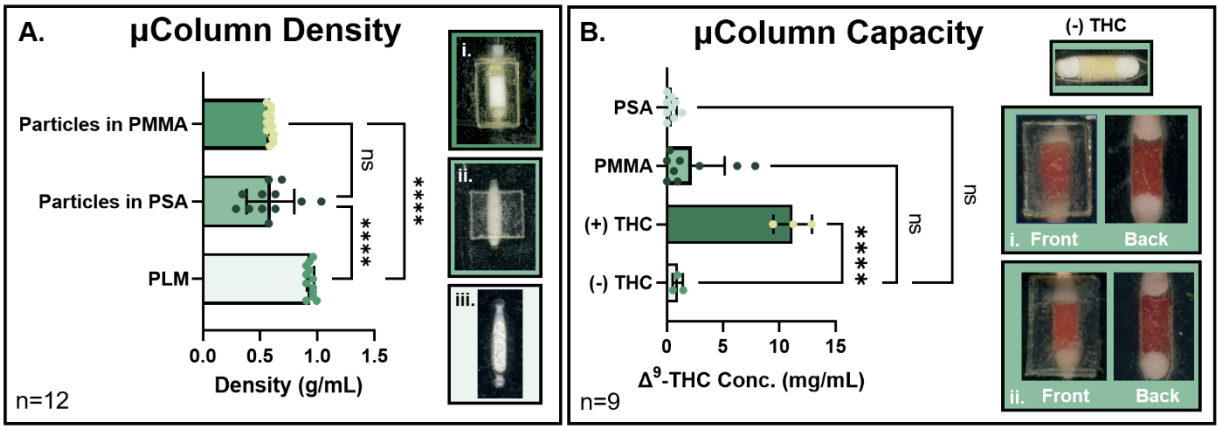


**Supplementary Figure 4:** *Evaluation of Packed Bed and Particle Loaded Membrane µColumns* (*Mean ± SD*). **A.** To compare µColumn density across separate fabrication methods, three distinct grids composed of 12 µColumn cavities were laser-cut and assembled according to the PCL method. Each cavity was composed of either 40-63 µm diameter $C_{18}$-functionalized silica particles packed within a **i.** PMMA or **ii.** PSA receptacle or a **iii.** 12 µm diameter $C_{18}$-functionalized silica particles within a PTFE fibril network (90% silica particles, 10% PTFE fibrils) Particle Loaded Membrane (PLM). Prior to the addition of functionalized microparticles, a (0.4 mm thick x 1.4 mm diameter) sintered polyethylene frit (pore size <25 µm) was wedged securely between microdevice layers 1 and 5, directly above and below the µColumn cavity (Figure 3A i-ii). After lamination, laser cut PMMA or PSA borders were affixed to each of 12 points within their respective grids. Excess microparticles were removed using a clean razor after dry packing. Finally, an overlay of PET with PSA adhesive was used to seal each µColumn. No attached receptacle was needed for the membrane, which was laminated directly within the main microdevice layers. The mass within each µColumn was compared using a fine mass balance and simplified five-layer microdevice. A Multiple Comparisons ANOVA was performed to determine whether the mean densities between the various packing methods or materials differed significantly ($\alpha = 0.01$). **B.** The retention capabilities of $C_{18}$-functionalized silica particles for $\Delta^9$-THC were compared for two integrated µColumns with separate cross-sectional areas. **i.** "PMMA" µColumns had an expected cross-sectional area of 2.75 $mm^2$ while **ii.** "PSA" µColumns had an expected cross-sectional area of 0.8 $mm^2$. Each dry-packed particle µColumn was assessed using a simplified centrifugal microdevice. Column conditioning was achieved by the addition of 40 µL of $CH_3OH$ to the sample inlet followed by disc spinning at 3,000 RPM for 10 sec. This step

Supplementary Figures

was repeated with MQ $H_2O$. All conditioning reagents were automatically directed toward a waste chamber within the microdevice. Once conditioned, the channel leading to the waste chamber was closed through laser occlusion, and a valve below the column opened via brief laser ablation. 50 µL of 10% (v/v) $CH_3COOH$ in MQ $H_2O$, spiked with $\Delta^9$-THC to a final concentration of 10 mg/mL, was added to the sample inlet then spun through the µColumn at 3,000 RPM for 10 sec. The aqueous eluent was recovered from the disc, vacufuged to dryness, then reconstituted in $CH_3OH$ to ensure detectability before evaluation on Whatman 1 cellulose inserts pretreated with [1 M] NaOH. The hue values of aqueous eluent from each µColumn type, after reaction with Fast Blue B (FBB) azo dye, were evaluated via image analysis in reference to a negative and positive control. Concentrations were calculated according to a previously generated calibration curve (Supplementary Figure 10). A Multiple Comparisons ANOVA was performed to determine whether either µColumn type displayed evidence of $\Delta^9$-THC within the eluent ($\alpha = 0.01$). Insets display scanned images of the µColumns after reaction to FBB.

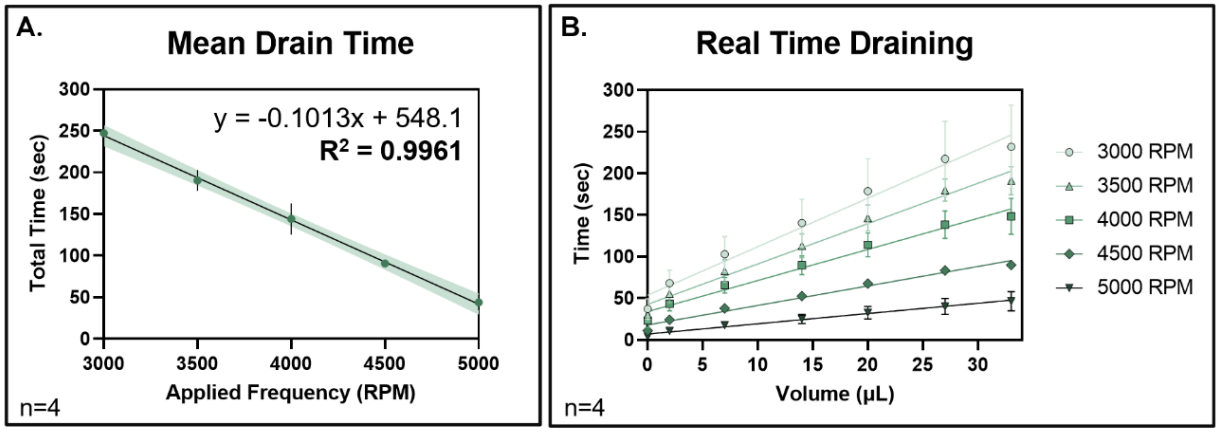


| C. Spin Frequency | Lin. Reg. Curve | $R^2$ Value |
|---|---|---|
| 3000 RPM | y = 5.830x + 53.63 | 0.9954 |
| 3500 RPM | y = 4.851x + 42.65 | 0.9936 |
| 4000 RPM | y = 3.736x + 33.93 | 0.9958 |
| 4500 RPM | y = 2.343x + 17.93 | 0.9951 |
| 5000 RPM | y = 1.232x + 7.034 | 0.9858 |

**Supplemental Figure 5.** *Flow Rate Characterization of Integrated µColumn* (*Mean ± SD*). Raw flow rate data derived from high-speed video monitoring. **A.** The mean drain time and **B. r**eal-time volumetric draining (µL/sec) across a frequency range of 3-5,000 RPM were both fit according to a linear regression curve ($R^2 = 0.9961$ for the mean drain time). Shading around the curve represent the 95% Confidence Interval (CI) around the line of best fit. **C.** The corresponding linear equations and associated $R^2$ values, per applied frequency, for real-time volumetric draining.

Supplementary Figures

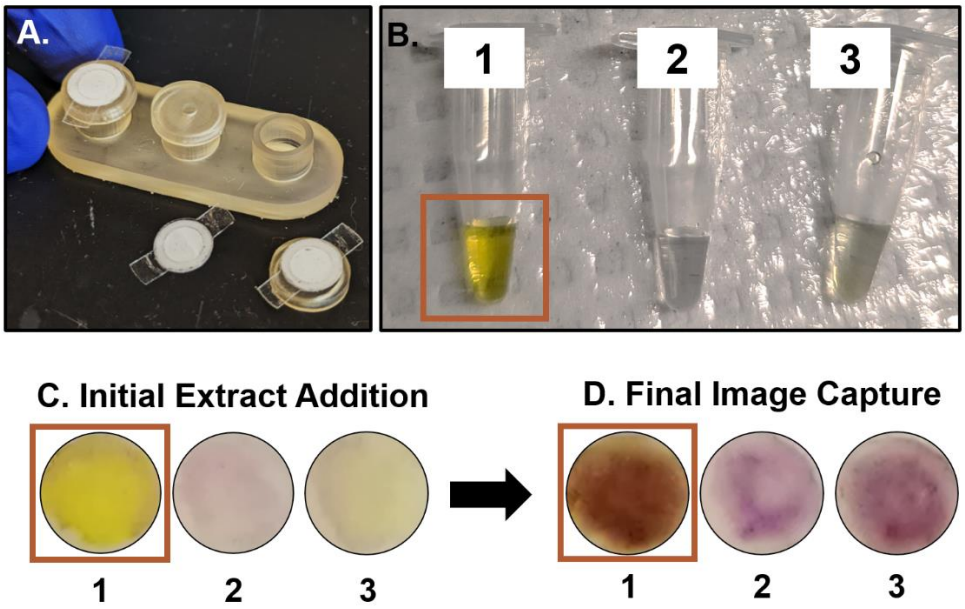


**Supplemental Figure 6.** *Sample Discoloration During CCD Extraction Optimization Study.* **A.** Image of actual 3D printed extraction chamber composed of triplicate chambers with separate vented lids. A removable PTFE membrane (white circle) allows only gas exchange during microwave heating. **B.** Example image of three replicates for one CCD condition (Condition 4: pH 1, 58 °C temperature, 309 sec dielectric heating time) immediately after microwave-assisted incubation. Samples were temporarily removed from their corresponding 3D printed extraction container and placed within separate 0.2 mL PCR tubes for imaging. Red box highlights replicate with significant discoloration. **C.** Image capture of all three replicates on detection pad immediately after addition (time: 0 sec). **D.** Image capture of all three replicates on detection pad at detection time point (180 sec post addition). Numbers and highlight correspond to identical replicate across all panels. Prior to removal of replicate 1, the average hue and standard deviation across all replicates was 125 ±14.8, with an associated average saturation 106 ± 64.2. Individually, the saturation values were measured to be: 179.5, 60.4, and 78.6. After removal of replicate 1, the average hue value shifted to 117, while the associated average saturation value shifted to 76.

Supplementary Figures

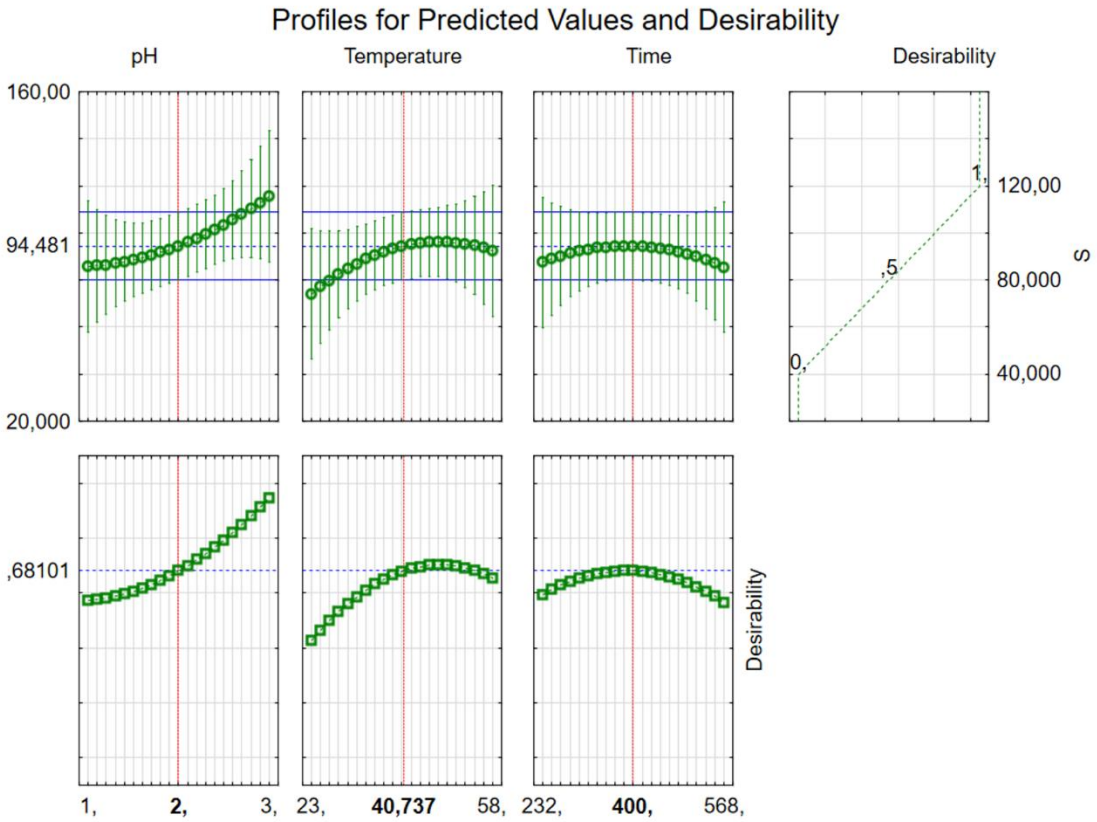


**Supplemental Figure 7.** *CCD Desirability Function for Extraction Optimization.* Profiles for predicted values and desirability function for the maximum extraction efficiency of codeine. Dotted red lines indicate the optimization values for pH, temperature, and time.

Supplementary Figures

**A.**

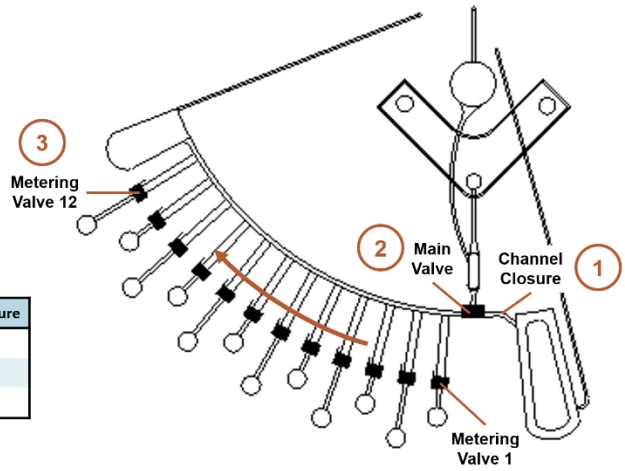


**B. Laser Diode Settings**

| | Valve Opening | Channel Closure |
|---|---|---|
| Laser Power (mW) | 400 | 600 |
| Exposure Time (ms) | 500 | 2500 |
| Laser Z-height(mm) | 15.0 | 29.0 |

**C.**

| Domain 1 | Angles (Deg) | Domain 2 | Angles (Deg) | Domain 3 | Angles (Deg) | Domain 4 | Angles (Deg) |
|---|---|---|---|---|---|---|---|
| M1 | 5.8 | M1 | 95.3 | M1 | 185.3 | M1 | 275.3 |
| M2 | 10.6 | M2 | 100.1 | M2 | 190.2 | M2 | 280.1 |
| M3 | 15.5 | M3 | 105.0 | M3 | 195.0 | M3 | 285.0 |
| M4 | 20.5 | M4 | 109.8 | M4 | 199.8 | M4 | 289.8 |
| M5 | 25.2 | M5 | 114.7 | M5 | 204.7 | M5 | 294.7 |
| M6 | 30.0 | M6 | 119.5 | M6 | 209.5 | M6 | 299.5 |
| M7 | 34.9 | M7 | 124.4 | M7 | 214.4 | M7 | 304.4 |
| M8 | 39.7 | M8 | 129.2 | M8 | 219.2 | M8 | 309.2 |
| M9 | 44.5 | M9 | 134.5 | M9 | 224.0 | M9 | 314.0 |
| M10 | 49.5 | M10 | 139.4 | M10 | 228.9 | M10 | 318.9 |
| M11 | 54.2 | M11 | 143.7 | M11 | 233.7 | M11 | 323.7 |
| M12 | 59.1 | M12 | 148.6 | M12 | 238.6 | M12 | 328.6 |
| Channel Closure: | 357.5 | | 87.5 | | 177.5 | | 267.5 |
| Main Valve: | 0.7 | | 90.7 | | 181.0 | | 271.2 |

| | |
|---|---|
| Channel Closure: | 43.5 |
| Main Valve: | 43.0 |
| Metering: | 53.0 |

**Supplemental Figure 8.** *Microdevice Automated Valving*. **A.** AutoCAD rendering of a single domain is provided to illustrate valve identity within the integrated microdevice design. The order of valve engagement (per domain) is shown via the numbers highlighted in red. **B.** Inset table provides settings for the laser diode for both opening and channel closure. **C.** Main table containing all necessary information to achieve automated valving using the custom micromechanical platform (see **Supp. 2**) across all four domains of the integrated microdevice. All distances from the center of rotation are in millimeters. The optical switch (right side) serves as the zero angle reference. All angles are measured clockwise from the reference angle. Angles are in degrees.

**Microwave-Assisted Extraction, Separation, and Chromogenic Detection of Laced Marijuana for Presumptive Point-of-Interdiction Testing**

*O'Connell, K.; et al.*

Supplementary Figures

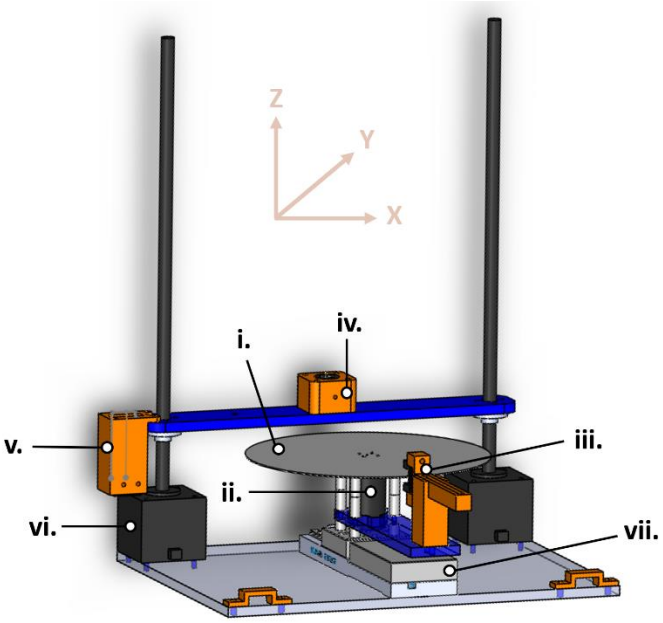


**Supplemental Figure 9.** *Custom Micromechanical System for Automated Laser Valving and Fluidic Drive.* SolidWorks rendering of custom micromechanical platform with **i.** a centrifugal disc attached to the **ii.** brushless motor. **iii.** An infrared optical switch detects the laser-cut 'optical notch' on the disc edge, used to provide real-time disc orientation feedback for automated valving. **iv.** A 3D-printed housing for the laser diode is mounted on a gantry, which is controlled by **v.** a z-height calibrator and **vi.** two servo motors. **vii.** The laser distance from the center of the disc is controlled separately by a third servo motor mounted in the x-axis.

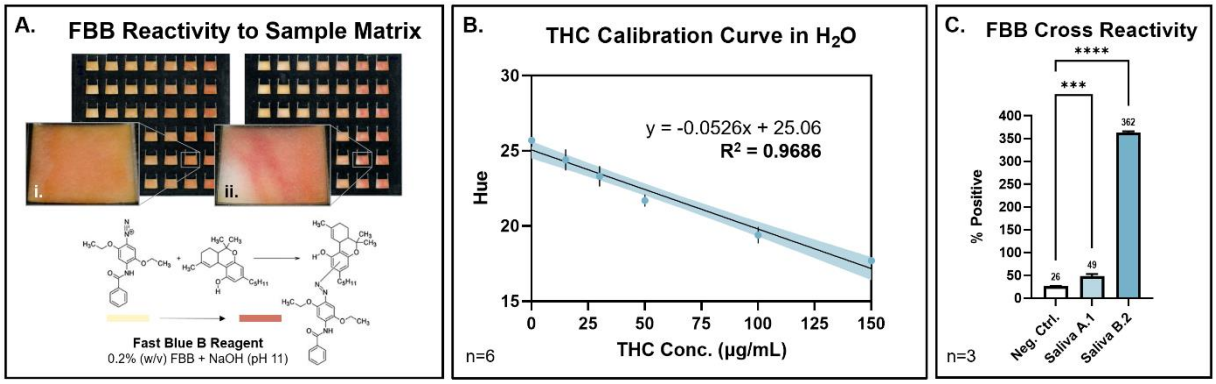


**Supplementary Figure 10.** *False Positive Potential with Δ⁹-THC Detection Reagent* (*Mean ± SD*). **A.** Image of calibration curve comparison with Fast Blue B (FBB) azo dye pre-stored within a Whatman 1 cellulose insert against Δ⁹-THC that was serially diluted in either **i.** methanol or **ii.** water. The visibly apparent difference in hue and chromogenic response surface pattern are highlighted. Reaction below illustrates formation of diazonium complex with Δ⁹-THC along with the expected change in hue. The grid was subsequently scanned using a desktop scanner and analyzed for hue within the HSB color model in Fiji. **B.** Calibration curve of FBB with Δ⁹-THC spiked within MQ $H_2O$ across a concentration range of 15-150 µg/mL. A linear regression curve was fit to the resulting hue measurements (R2 = 0.9686). Shading along the curve represents the 95% Confidence Interval (CI) around the line of best fit. **C.** Example of cross reactivity observed for FBB against phenolic analogs derived from tea drinking. A negative control (Neg. Ctrl.) composed of MQ $H_2O$ was included as a baseline reference. Two individuals (designated A.1 and B.2) were instructed to rinse with tap water for 30 sec prior to the collection of neat oral fluid (OF) samples. No food or beverages, beyond water, were consumed for at least 1 hr prior to OF collection. Individual B.2 was additionally instructed to consume 8 oz of green tea just prior to the 1 hr waiting period. Both individuals self-reported no recent coffee consumption or marijuana use for a minimum of 2 weeks prior to testing. Immediately after OF collection, both samples were spiked with 30 µg/mL Δ⁹-THC to ensure any Δ⁹-THC content below the limit of quantitation was detectable. A test grid, identical to the version described previously, was used for evaluation of Δ⁹-THC concentration. Measured Δ⁹-THC concentration was calculated using the previously established calibration curve. A Multiple Comparisons One-Way ANOVA was performed to determine whether the mean Δ⁹-THC content detected within the saliva

Supplementary Figures

samples differed significantly from 30 µg/mL (α = 0.01). All OF samples were collected in accordance with the procedures approved by the Institutional Review Board (IRB, Num. 19947).

A.

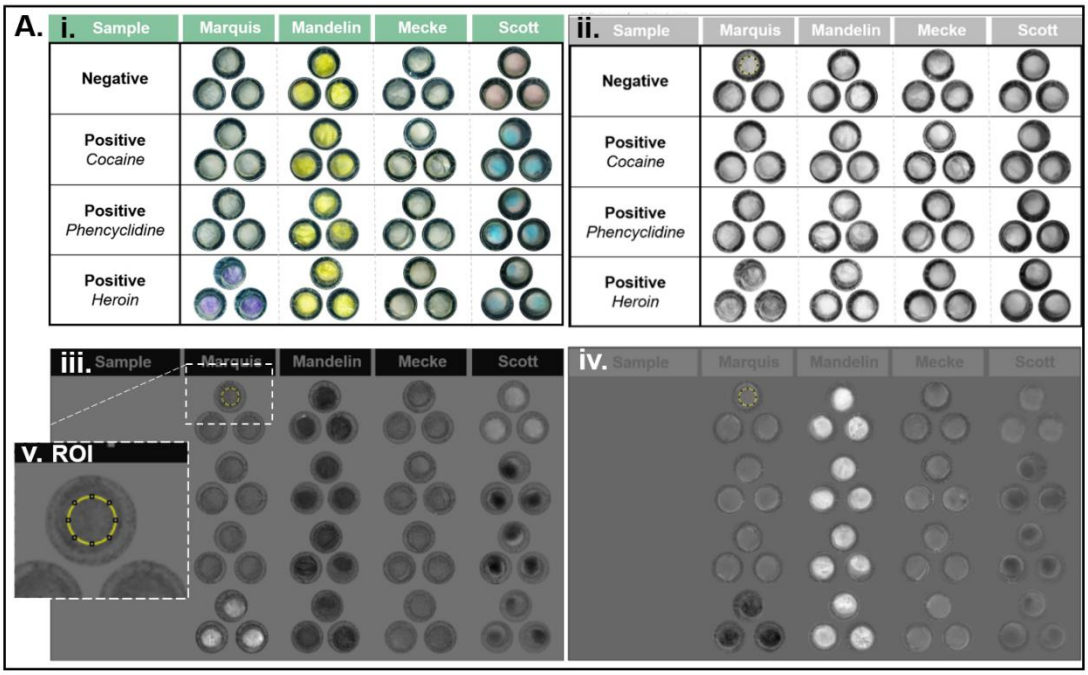


B.

| Cluster | 1 | 2 | 3 | 4 | 5 |
|---|---|---|---|---|---|
| **Number of Objects by Cluster** | 6 | 3 | 6 | 12 | 12 |
| **Sum of Weights** | 6 | 3 | 6 | 12 | 12 |
| **Within-Cluster Variance** | 0.209 | 0.236 | 0.351 | 8.157 | 1.359 |
| **Minimum Distance to Centroid** | 0.152 | 0.189 | 0.245 | 1.833 | 0.827 |
| **Average Distance to Centroid** | 0.381 | 0.373 | 0.499 | 2.609 | 1.104 |
| **Maximum Distance to Centroid** | 0.687 | 0.511 | 0.786 | 4.118 | 1.370 |
| | Blank | THC | Amp | Heroin | Cocaine |
| | Blank | THC | Amp | Heroin | Cocaine |
| | Blank | THC | Amp | Heroin | Cocaine |
| | **Negative** | | Meth | **H** | **C** |
| | **Negative** | | Meth | **H** | **C** |
| | **Negative** | | Meth | **H** | **C** |
| | | | | Codeine | PCP |
| | | | | Codeine | PCP |
| | | | | Codeine | PCP |
| | | | | MDMA | **P** |
| | | | | MDMA | **P** |
| | | | | MDMA | **P** |

## Supplementary Figures

**Supplemental Figure 11.** *Objective image data curation for PCA and AHC.* **A.** Cropped, magnified, and compiled images of all detection wells (top view). Each row denotes either the negative control or illicit lacing agent, with columns denoting the indicator reagent. The **i.** original RGB image was imported into Fiji before conversion to a CIELAB stack (**ii.** L*, **iii.** a*, and **iv.** b*). **v.** Inset displays the 40x40 region of interest (ROI) overlay used across all samples. **B.** Summary of AHC results by cluster. Bolded labels indicate on-disc samples.